

JGR Space Physics

RESEARCH ARTICLE

10.1029/2019JA027768

Key Point:

- There is evidence of enhanced electron densities in the near-moon environment when Enceladus is in the post-apoapsis sector of its orbit

Supporting Information:

- Supporting Information SI

Correspondence to:

A. M. Persoon,
ann-persoon@uiowa.edu

Citation:








Persoon, A. M., Kurth, W. S., Gurnett, D. A., Groene, J. B., Smith, H. T., Perry, M. E., et al. (2020). Evidence of electron density enhancements in the post-apoapsis sector of Enceladus' orbit. *Journal of Geophysical Research: Space Physics*, 125, e2019JA027768. <https://doi.org/10.1029/2019JA027768>

Received 2 JAN 2020

Accepted 7 MAY 2020

Accepted article online 17 MAY 2020

Evidence of Electron Density Enhancements in the Post-Apoapsis Sector of Enceladus' Orbit

A. M. Persoon¹ , W. S. Kurth¹ , D. A. Gurnett¹ , J. B. Groene¹ , H. T. Smith²,
M. E. Perry² , M. W. Morooka³ , and S. Ye^{1,4} 

¹Department of Physics and Astronomy, University of Iowa, Iowa City, IA, USA, ²Applied Physics Laboratory, Johns Hopkins University, Laurel, MD, USA, ³Swedish Institute of Space Physics, Uppsala, Sweden, ⁴Now at Department of Earth and Space Sciences, Southern University of Science and Technology, Shenzhen, China

Abstract Enceladus' plume is the dominant source of neutrals and plasma in Saturn's magnetosphere. The plasma results from the ionization of icy particles and water vapor, which are vented into Saturn's inner magnetosphere through fissures in Enceladus' southern polar region. These fissures are subjected to tidal stresses that can vary as Enceladus moves in a slightly eccentric orbit around Saturn. Plume activity and brightness have also been shown to vary with the moon's orbital position, reaching a maximum when Enceladus is farthest away from Saturn in its orbit (the Enceladus orbital apoapsis). In this paper we will show that temporal variations in the thermal electron density distribution correlate with the position of Enceladus in its orbit around Saturn, with the strongest density enhancements in the vicinity of Enceladus when the moon is in the post-apoapsis sector of its orbit.

1. Introduction

Early Cassini observations revealed a plume consisting of sprays of icy particles and water vapor, erupting from fissures called tiger stripes in Enceladus' southern polar region and venting into Saturn's neutral torus (Dougherty et al., 2006; Hansen et al., 2006, 2011; Hedman et al., 2009; Johnson et al., 2006; Porco et al., 2006; Waite et al., 2006, 2009). This geological activity has been associated with the diurnal cycling of the tidal stresses acting on Enceladus as the moon moves in its slightly eccentric orbit around Saturn (Hurford et al., 2012; Spencer, 2013).

An analysis of the normal tidal stresses has shown that these stresses vary in strength as Enceladus orbits Saturn (Hurford et al., 2007). The normal tidal stresses are the driving mechanism for the eruptions in the southern polar region (Porco et al., 2014), acting to alternately widen and compress segments of the tiger stripes, potentially increasing and then decreasing the ejection of gas and icy particles during the moon's orbital cycle. These tidal stresses put the cracks under the most tension when Enceladus is farthest away from Saturn (apoapsis), where they act to widen the fissures in the southern polar region. When Enceladus is closest to Saturn (periapsis), the tidal stresses are at maximum and act to compress the fissures (Hurford et al., 2007). Shear tidal stresses also contribute to the eruption activity by driving strike-slip motion along the fissures, resulting in shear heating and potentially contributing to the action of the normal stresses on the tiger stripes (Nimmo et al., 2007; Smith-Konter & Pappalardo, 2008). The analyses of these tidal stresses infer potential perpendicular and parallel movement along the tiger stripes that drive eruption activity in the southern polar region (Hurford et al., 2007; Porco et al., 2014).

The temporal variability of the tidal stresses acting on the tiger stripes was expected to produce temporal variations in the plume and in the flux of neutral particles and gas being emitted from those fissures. Early evidence for the temporal variability of Enceladus' neutral environment was reported by Saur et al. (2008), who found that the neutral density and flux decreased by a factor of 10 during the first three Cassini flybys. Smith et al. (2010) modeled neutral water group densities against the peak neutral water densities measured by the Ion and Neutral Mass Spectrometer (INMS) for three inclined flybys and showed that the neutral source rate was variable by a factor of four during the 7-month period of the study.

A correlation between the variability in the neutral densities and source rate with variations in the Enceladus plume activity was shown when later studies found an orbital-dependent variation in the plume activity. Observations of Enceladus' plume found that time variations in the brightness of the plume

correlated with Enceladus' orbital position (Hedman et al., 2013; Nimmo et al., 2014) and supported the tidal-opening model for normal stresses acting on the tiger stripes in the southern polar region (Hurford et al., 2007). Variations in the plume brightness and total particle flux by the Imaging Science Subsystem (ISS) and the Visual and Infrared Mapping Spectrometer (VIMS) confirmed that the brightness of the plume, formed by the icy particle sprays, is greatest when Enceladus is at apoapsis, where normal tidal stresses act to widen the fissures. The plume is dimmer when Enceladus is at periapsis and the fissures are under compression (Hedman et al., 2013; Hurford et al., 2007; Nimmo et al., 2014). Using 10 years of Enceladus flyby data, Ingersoll and Ewald (2017) also found that plume brightness at all altitudes up to 200 km was up to five times brighter when Enceladus was near apoapsis than it was near periapsis, confirming the earlier results of Hedman et al. (2013).

INMS measurements of several highly volatile species in the plume spray were also found to exhibit the same orbital dependence as the plume variability, with count rates peaking during the E17 and E18 Cassini flybys of Enceladus near apoapsis (Perry et al., 2015). However, the orbital dependence of the plume vapor variability was not supported in a later study by Hansen et al. (2017), who used measurements from the Ultraviolet Imaging Spectrograph (UVIS) to determine that water vapor in the Enceladus plume did not vary significantly with the moon's orbital position. They further postulated that localized supersonic gas jets, and not the broader vapor emissions from the tiger stripes, were the source of the observed particle flux variability. INMS data and UVIS occultation measurements of the water vapor column density were used to study the variability of the gas jets and the interjet vapor emissions. Teolis et al. (2017) found that spatial and time variability of the vapor plume source rate is similar to the spatial and time variability of the 98 individual gas jets previously identified by Porco et al. (2014). A different model was proposed by Yeoh et al. (2017) who determined that distributed sources along the tiger stripes are the dominant sources of the plume vapor and particles and that the jets provided lesser, more localized, density enhancements.

The objective of this study is to determine whether variations in the distribution of the thermal electron densities in the moon's near environment exhibit an orbital-phase dependence. The electron density, n_e in cm^{-3} , is derived from the peak frequency, f_{UH} , of the narrowband upper hybrid emissions detected by the Cassini Radio and Plasma Wave Science (RPWS) instrument (Persoon et al., 2005). The density measurements are computed using $n_e = (f_{UH}^2 - f_c^2) / (8980)^2$ where f_c is the electron cyclotron frequency and all frequencies are given in Hz. The average uncertainty of these density measurements is $\sim 15\%$. The RPWS density measurements and their associated uncertainties are available at the Planetary Data System (see the Acknowledgments section).

The study focuses on Enceladus' immediate environment, using electron density measurements from all of the Cassini equatorial flybys through the Enceladus plume to map the distribution of the thermal electrons below the ring plane near the moon. Equatorial flybys are defined to be flybys within 2.4 Enceladus radii (R_E) of the moon's orbital plane. Limiting the study to only equatorial flybys eliminates the strong latitudinal dependence of the density distribution (in a Saturn-centered equatorial coordinate system) and focuses on the radial dependence of the electron distribution. The study will utilize electron density measurements within 200 Enceladus radii (R_E) of the moon and map the densities as a function of Enceladus' position in its orbit around Saturn. Because of intense dust impacts on the electric antennas which obscure the much-fainter upper hybrid emissions (Ye et al., 2014), most of the RPWS density measurements of the free thermal electrons are obtained outside the central plume region beginning at distances $\geq 1.2 R_E$. Few density measurements are available inside the plume.

2. Electron Density Distributions in the Near Vicinity of Enceladus

To investigate the density fluctuations in the vicinity of Enceladus, the study uses electron density measurements obtained during the Cassini flybys of the moon. There were a total of 23 flybys of Enceladus during the Cassini mission. Of these 23 flybys, six of them are highly inclined trajectories (E2, E3, E4, E5, E6, and E11) which are not included in this study in order to compare electron densities without a strong latitude dependence. Cassini passed over the northern polar region on four flybys (E0, E12, E13, and E20). On the remaining 13 flybys, Cassini passed through the Enceladus plume and remained within 2.4 R_E of Enceladus' orbital plane in the near-moon environment. This study will focus on these 13 equatorial flybys over the moon's southern polar region. The flyby trajectories, shown in Figure 1, provide the most complete set of density

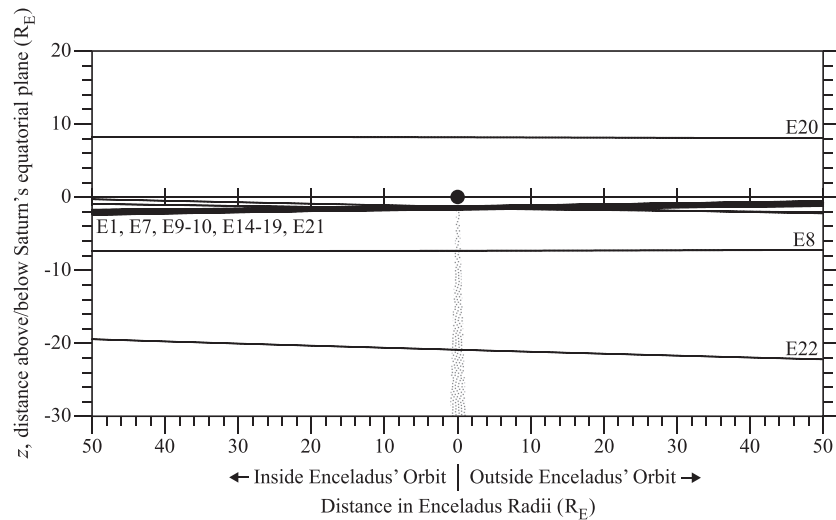


Figure 1. Cassini trajectories through the Enceladus plume within 50 moon radii for 13 equatorial flybys. Also shown is the Cassini flyby over Enceladus' northern polar region when Enceladus was near periapsis (E20).

measurements in the equatorial plane over a range of radial distances before and after the closest approach to Enceladus in the plume region. Cassini crossed above Enceladus' southern polar region at altitudes ranging from 52 to 5,000 km. Only one of the equatorial flybys (E20) occurred when Enceladus was close to Saturn (periapsis). In the E20 flyby, Cassini passed over Enceladus' northern polar region at an altitude of 1,844 km. This flyby is included to establish a background electron density in the near-moon environment at a time when plume activity is minimal and Cassini is more than 2,000 km downstream of any plume effects. Note that 11 of these flybys occur within 500 km of the moon's surface. E8 and E22 are the most distant flybys and are discussed separately in section 3. Table 1 is a listing of these 14 Enceladus flybys along with the corresponding orbit number, the time of Cassini's closest approach to the moon, the altitude of Cassini at the time of closest approach and the orbital phase of Enceladus at the time of closest approach (see discussion below).

Figure 2 shows the radial distribution of more than 17,000 RPWS equatorial electron density measurements obtained during the 13 Cassini equatorial flybys of Enceladus inside 200 R_E . Density measurements taken during the Cassini flyby over the northern polar region when Enceladus is near periapsis (E20) are shown in black. Overall, the E20 densities are very consistent, ranging between 50 and 70 cm^{-3} , both inside and outside Enceladus' orbit. There is a strong E20 density increase over the northern polar region at $\sim 10 R_E$ which may be due to secondary ejecta plasma (Farrell et al., 2010, 2012; Kempf et al., 2010). Secondary ejecta are a common feature in electron density distributions close to Enceladus' surface and are not directly dependent on the moon's orbital position.

In Enceladus' southern hemisphere, there are density dropouts inside the edges of the plume region and frequent electron density spikes at the plume boundaries. The density dropouts inside the plume region are attributed to electron absorption by the dust particles ejected from fissures in Enceladus' southern polar region (Farrell et al., 2009, 2010; Hill et al., 2012; Morooka et al., 2011; Shafiq et al., 2011; Wahlund et al., 2009; Yaroshenko et al., 2009; Ye et al., 2014). Outside the plume, densities in the immediate vicinity of Enceladus are highly variable by up to a factor of three due, in part, to interactions between the plasma and icy grains (dust) in the near-moon environment. This study shows that the orbital position of the moon at the time the measurements were taken is also contributing to this density spread.

Table 1
Cassini Equatorial Flybys through Enceladus' Plume

Flyby	Orbit	Closest approach time	C/A altitude (km)	Orbital phase at C/A (°)
E1	4	2005-068 09:08:02	497.1	155.3
E7	120	2009-306 07:41:58	98.9	264.5
E8	121	2009-325 02:09:56	1596.6	150.5
E9	130	2010-118 00:10:17	100.4	186.4
E10	131	2010-138 06:04:40	437.1	99.1
E14	154	2011-274 13:52:26	98.9	241.9
E15	155	2011-292 09:22:12	1230.8	235.9
E16	156	2011-310 04:58:53	496.6	231.5
E17	163	2012-087 18:30:09	74.2	199.2
E18	164	2012-105 14:01:38	74.1	193.3
E19	165	2012-123 09:31:29	73.1	187.8
E20	223	2015-287 10:41:30	1844.2	338.2
E21	224	2015-301 15:22:47	52.4	103.7
E22	228	2015-353 17:49:20	5000.4	94.4

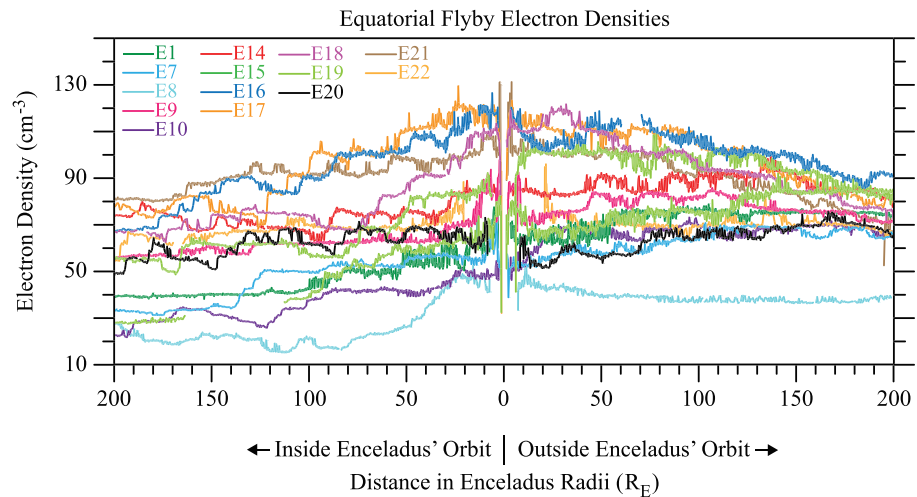


Figure 2. RPWS electron density measurements within 200 moon radii, both inside and outside the Enceladus orbit for the 14 flybys illustrated in Figure 1. The periapsis densities (in black) are fairly constant throughout the near-moon environment. The remaining density measurements are highly variable, particularly inside the Enceladus orbit.

3. Enceladus' Orbital Position During the Cassini Flybys

Figure 3 illustrates the position of Enceladus in its orbit around Saturn at the time of Cassini's closest approach for the 14 flybys shown in Figure 2. Enceladus' orbital phase, also known as the Enceladus mean anomaly, is computed in the direction of Enceladus' orbital motion from Enceladus' periapsis to the position of the moon in its orbit at the time of Cassini's closest approach to the moon. The orbital phase λ is 0° at periapsis and 180° at apoapsis and the moon's position coordinates are given in a Saturn-centered equatorial coordinate system, with position coordinates derived from the SPICE kernels. Information on locating the SPICE kernels for each of the Enceladus flybys can be found in Supporting Information Table S2. Thirteen of the Cassini equatorial flybys have closest approaches to the moon over a wide range of orbital phase in the pre-apoapsis and the post-apoapsis sectors of the orbit. Only E20 occurs within the $\pm 90^\circ$ sector from Enceladus' periapsis, when the tidal stresses are near maximum and the plume activity is expected to be minimal. The orbital phase values for these 14 equatorial flybys are listed in the final column of Table 1.

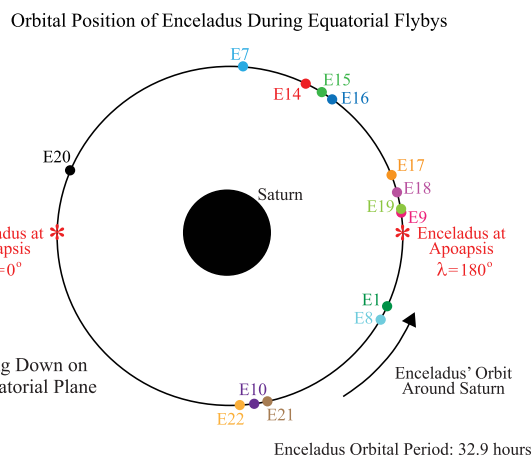


Figure 3. An illustration of Enceladus' position in its orbit around Saturn at the time of Cassini's closest approach to the moon for each of the 14 flybys illustrated in Figure 1. The orbital phase is computed in the direction of the moon's orbital motion from periapsis (at 0°) to the position of Cassini at closest approach. The orbital phase at apoapsis is 180° .

The electron density profiles shown in Figure 2 are now divided into a post-apoapsis panel (a) and a pre-apoapsis panel (b) in Figure 4. In the post-apoapsis panel, the three lowest density profiles are obtained during E7, E9, and E19. Enceladus has an orbital phase of 264.5° at closest approach for the E7 flyby, which shows no evidence of enhanced densities. E9 and E19 have orbital phases of 186.4° and 187.8° at closest approach with small density enhancements up to 80 cm^{-3} , within $10 R_E$ of the plume region. Stronger density enhancements occur for the remaining post-apoapsis orbits with orbital phases of 193° – 242° . Near closest approach, the densities for these post-apoapsis orbits range from 90 – 120 cm^{-3} and remain enhanced out to $100 R_E$.

Orbital phase does help to organize the highly variable electron densities in the near-moon environment. The densities in the pre-apoapsis sector in panel (b) are generally low, $\leq 60 \text{ cm}^{-3}$, at all radial distances from the moon. The exception is E21, which exhibits strong density spikes near the plume boundaries and consistently enhanced densities to beyond $100 R_E$. Strong density spikes near the plume boundaries are also evident in several other flybys in Figure 4b, although electron densities farther from the plume

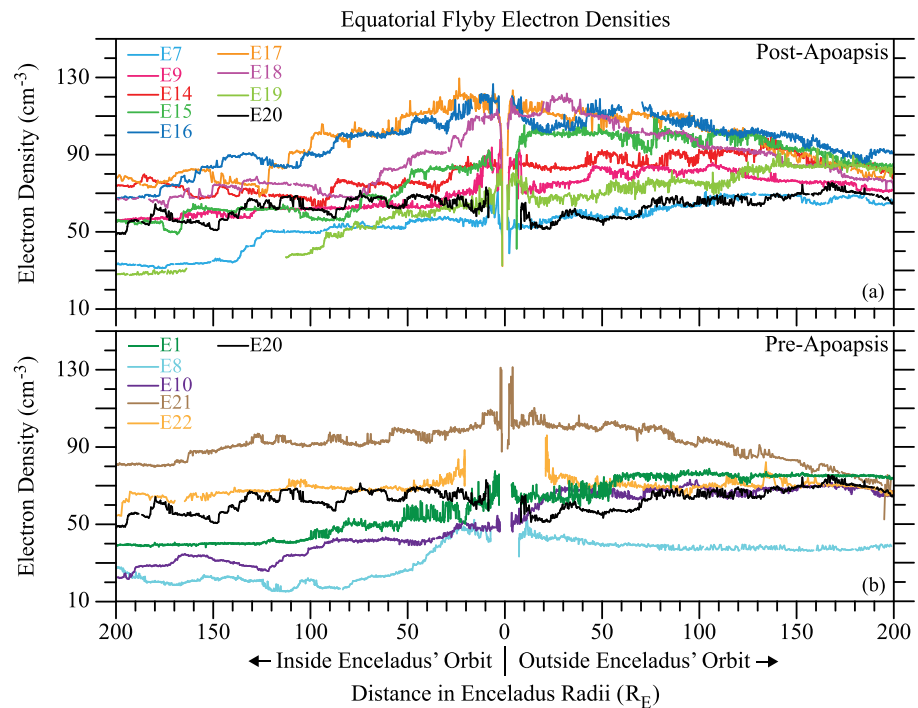


Figure 4. The RPWS electron density measurements within 200 moon radii, both inside and outside the Enceladus orbit, are separated into a post-apoapsis panel (a) and a pre-apoapsis panel (b). The E20 densities are shown in black in both panels to illustrate background electron density in the near-moon environment at a time when plume activity is minimal. In the post-apoapsis panel, E9 and E19 have strong density enhancements up to 80 cm^{-3} , within $10 R_E$ of the plume region. Stronger density enhancements occur for the remaining post-apoapsis orbits out to $100 R_E$ and more. The densities in the pre-apoapsis sector in panel (b) are generally low, $\leq 60 \text{ cm}^{-3}$, at all radial distances. The exception is E21, which exhibits strong density spikes near the plume boundaries and consistently enhanced densities to beyond $100 R_E$.

boundaries remain low. Note the strong density spikes near the plume boundaries for the E22 flyby. E22 is the most distant flyby through the plume region with a closest approach at $5,000 \text{ km}$ ($2.0 R_E$). The density spikes near the plume boundaries occur at $\sim 20 R_E$, illustrating the broad expansion of the plume at

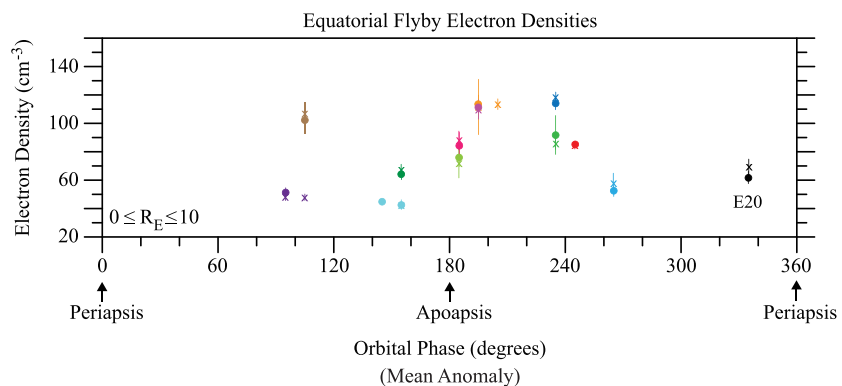


Figure 5. RPWS electron densities inside $10 R_E$ as a function of orbital phase for the 14 flybys, averaged in bins of 10° of orbital phase centered on Enceladus for measurements obtained both inside (indicated by an X) and outside (indicated by a circle) Enceladus' orbit. Note that some density symbols are obscured by other density symbols when the densities and orbital phases are closely matched. The density measurements are color-coded according to the color scale indicated in Figure 2. The error bars represent one-sigma standard deviation of the averaged density value. Often, these error bars are smaller than the diameter of the density symbols and cannot be seen. The density distribution shows a consistent and significant density increase of twice the E20 density value in the post-apoapsis sector between 180° and 245° .

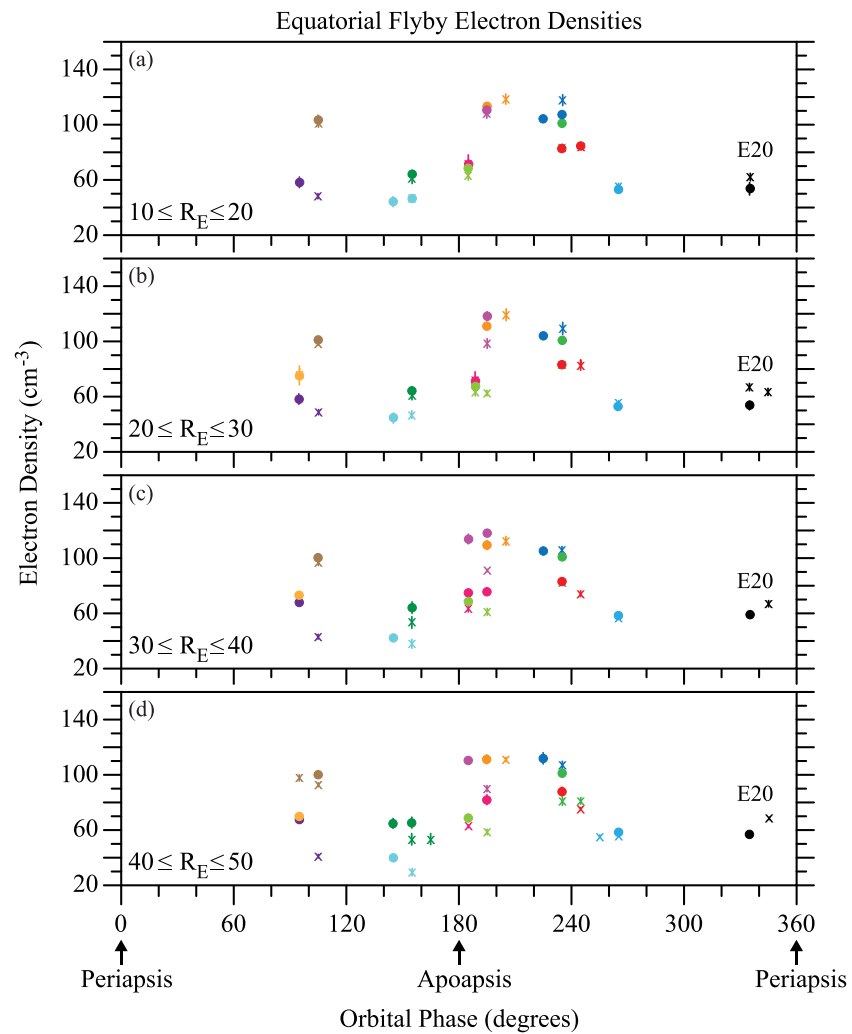


Figure 6. Averaged RPWS electron densities from 10 to 50 R_E as a function of orbital phase for the 14 flybys shown in Figure 5. The broad density enhancement observed inside 10 R_E in Figure 5 is consistently observed in the same orbital phase sector out to 50 R_E .

increasing distance from the moon's surface, compared with the E21 density spikes which occur inside 5 R_E . The E22 flyby is an example where the orbital phase is not the only factor which controls the density variability. Although E22 is the flyby farthest from the moon's surface, the E22 densities are two times higher than the E8 densities with a closest approach distance of 1,597 km (6.3 R_E). The plume region is highly dynamic and the densities are variable.

4. The Orbital Phase Dependence of the Electron Density Distributions

Figure 5 shows the RPWS electron density measurements inside 10 R_E as a function of orbital phase for all of the equatorial flybys. In this figure and in Figures 6–7, the densities are averaged in bins of 10° of orbital phase, centered on Enceladus. Density measurements are averaged both inside and outside the L -shell of Enceladus' orbit at 3.95 Saturnian radii (R_S) and, for Figure 5, include the density spikes and dropouts observed near the plume boundaries for each flyby trajectory. Averaged densities inside Enceladus' orbit are identified by X symbols and averaged densities outside Enceladus' orbit are identified by circles. The error bars represent one-sigma standard deviation of the averaged density values. In Figure 5, the electron

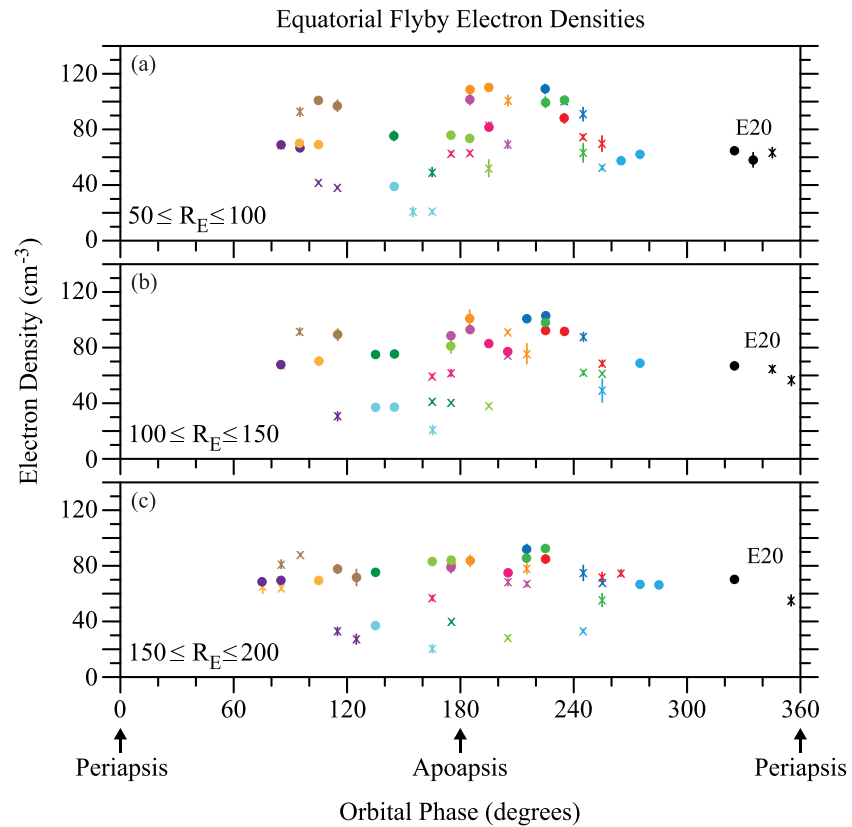


Figure 7. Averaged RPWS electron densities from 50 to 200 R_E as a function of orbital phase for the 14 flybys shown in Figure 5. The evidence of enhanced densities in the post-apoapsis sector still exists inside 100 R_E . There is no strong orbital phase dependence in the electron distribution outside 100 R_E .

density measurements show strong evidence for a broad enhancement in the post-apoapsis sector. The electron distribution in this sector shows a consistent and significant density increase of twice the E20 density value between 180° and 245°. Outside this range of orbital phase values, the density measurements for all but one flyby are $\leq 65 \text{ cm}^{-3}$, consistent with electron density measurements near Enceladus' periapsis (E20). A density spike, attributed to the E21 flyby, occurs at an orbital phase of $\sim 104^\circ$ and does not match the expected diurnal variations with Enceladus' orbital period. One possible explanation for this density enhancement in the pre-apoapsis sector is Cassini's close proximity to Enceladus. During this flyby, Cassini passed within 52 km of the moon's southern polar surface, making this the closest flyby over the tiger stripes. Ingersoll et al. (2019) found other factors contributing to the high variability of particle densities in the near-moon environment. Decadal variability in the plume brightness associated with the Enceladus-Dione resonance and aperiodic variations in gas jet activity attributed to changes in Enceladus' internal plumbing may also be associated with density enhancements outside the post-apoapsis sector.

Figure 6 is a four-panel plot of the RPWS equatorial electron density measurements from 10–50 R_E as a function of orbital phase. The density distribution in this near-Enceladus environment remains identical to the density distribution inside 10 R_E . There is a broad density enhancement in the post-apoapsis sector between 180° and 245° out to 50 R_E , with densities consistently enhanced above the E20 periapsis densities. In the pre-apoapsis sector, the E21 density spike can still be observed out to 50 R_E , but the remaining densities in the pre-apoapsis sector are consistent with the E20 density measurements.

Beyond 50 R_E , the electron distribution begins to change as the plasma, under the influence of the centrifugal force of the rotating plasma disk, expands outward from the plasma source and diffuses inward to merge with the ring plasma in the inner magnetosphere (Persoon et al., 2013, 2009). Figure 7 is a three-panel plot of the RPWS electron density measurements from 50–200 R_E as a function of orbital phase for all of the

equatorial flybys through the plume. Although all of the density measurements show roll-off with increasing distance from Enceladus and the orbital phase of the density measurements begins to change, evidence of enhanced electron densities post-apoapsis still persists inside $100 R_E$. Beyond $100 R_E$, the density enhancement in the post-apoapsis sector is beginning to break down. Beyond $150 R_E$, there is no strong evidence of orbital phase dependence in the electron distribution. The electrons at all orbital phase values have merged with the background E-ring population with densities consistent with the modeled plasma density distribution in Saturn's inner magnetosphere at $L = 4$ (Persoon et al., 2013). Because the averaged density values and the smaller error bars can frequently overlap, all of the information presented in Figures 5–7 is available in Table S1 in the Supporting Information.

5. Discussion

The consistent and significant electron density enhancement in the post-apoapsis sector of Enceladus' orbit strongly indicates an orbital phase dependence. However, the link between these enhanced electron densities just beyond the plume region and the phase-dependent particle flux in the plume region is not strongly correlated. ISS results clearly report a peak in the particle emissions closer to apoapsis than the peak in the enhanced electrons (Ingersoll & Ewald, 2017; Ingersoll et al., 2019), a delay that could be attributed to electron generation and transport processes.

The dominant ionization processes acting on the water molecules ejected from Enceladus are charge exchange (Johnson et al., 2006; Smith et al., 2010) and photo-induced processes, such as photodissociation and photoionization (Smith et al., 2010). While electron-impact ionization occurs in this region, most of the electrons near Enceladus have energies below the ionization cut-off, so only the higher-energy tail of the electron distribution causes ionization. Charge exchange and photodissociation of neutral water molecules do not produce free electrons and, hence, cannot account for the enhanced thermal electron population in the near-moon environment at apoapsis. Photoionization lifetimes are on the order of months and, with the moon's orbital period of 32.9 h, are too slow to account for noticeable electron density enhancements on the order of hours (Smith et al., 2010). Additionally, electrons drift through this near-moon environment in less than 100 s as they corotate with the magnetic field. While the occurrence of enhanced electron densities in this localized region makes a strong argument for an orbital dependence, there is no obvious ionization process to link the enhanced electron densities with the neutral densities associated with the neutral source rate increase at apoapsis.

It is possible that significantly enhanced neutral densities and/or extremely slow plasma speeds near Enceladus could dramatically increase ionization rates, resulting in an increase in the electron densities in the near-moon environment. Omidi et al. (2012) modeled the charge exchange between the corotating plasma and neutral gas emitted from fissures in Enceladus' southern polar region. In the charge exchange interaction, the hotter and faster corotating ions are replaced by colder and nearly stationary plume ions, resulting in a reduction in the plasma flow velocity which could increase plasma ionization rates. This stagnation in the flow velocity allows ion-molecule interactions to occur, reactions which result in positively and negatively charged particles, enhanced ion densities, and heavier cluster ions observed inside the Enceladus plume (Morooka et al., 2011; Tokar et al., 2009). Further electron absorption by icy dust particles in the plume region couples the negatively charged dust to the corotating plasma resulting in additional plasma deceleration (Omidi et al., 2012), further increasing the ionization rates. Sakai et al. (2016) investigated reduced plasma velocities using a Monte Carlo method that included a reduced electric field in the plume region and collisional processes, charge exchange and ion-neutral chemical reactions, to show even greater ion density increases in the highly collisional plume region. However, it is difficult to envision ionization rates increasing enough to double the electron density on the order of minutes to hours in the near-Enceladus environment. There may likely be another process or combination of processes that allows the electron population to respond so quickly. Further work is necessary to explain these enhanced electron densities and the orbital dependence of the thermal electron population in Enceladus' immediate environment.

Data Availability Statement

The RPWS electron density data used in this study are available at Planetary Data System (<https://doi.org/10.17189/1518302>).

Acknowledgments

The Cassini radio and plasma wave research at the University of Iowa is supported by NASA through JPL contract 1415150.

References

- Dougherty, M. K., Khurana, K. K., Neubauer, F. M., Russell, C. T., Saur, J., Leisner, J. S., & Burton, M. E. (2006). Identification of a dynamic atmosphere at Enceladus with the Cassini magnetometer. *Science*, *311*(5766), 1406–1409. <https://doi.org/10.1126/science.1120985>
- Farrell, W. M., Kurth, W. S., Gurnett, D. A., Johnson, R. E., Kaiser, M. L., Wahlund, J.-E., & Waite, J. H. Jr. (2009). Electron density dropout near Enceladus in the context of water-vapor and water-ice. *Geophysical Research Letters*, *36*, L12023. <https://doi.org/10.1029/2008GL037108>
- Farrell, W. M., Kurth, W. S., Tokar, R. L., Wahlund, J.-E., Gurnett, D. A., Wang, Z., et al. (2010). Modification of the plasma in the near-vicinity of Enceladus by the enveloping dust. *Geophysical Research Letters*, *37*, L11202. <https://doi.org/10.1029/2010GL044768>
- Farrell, W. M., Wahlund, J.-E., Morooka, M., Gurnett, D. A., Kurth, W. S., & MacDowall, R. J. (2012). The electromagnetic pickup of submicron-sized dust above Enceladus' northern hemisphere. *Icarus*, *219*(1), 498–501. <https://doi.org/10.1016/j.icarus.2012.02.033>
- Hansen, C. J., Esposito, L., Stewart, A. I. F., Colwell, J., Hendrix, A., Pryor, W., et al. (2006). Enceladus' water vapor plume. *Science*, *311*(5766), 1422–1425. <https://doi.org/10.1126/science.1121254>
- Hansen, C. J., Esposito, L. W., Aye, K.-M., Colwell, J. E., Hendrix, A. R., Portyankina, G., & Shemansky, D. (2017). Investigation of diurnal variability of water vapor in Enceladus' plume by the Cassini ultraviolet imaging spectrograph. *Geophysical Research Letters*, *44*, 672–677. <https://doi.org/10.1002/2016GL071853>
- Hansen, C. J., Shemansky, D. E., Esposito, L. W., Stewart, A. I. F., Lewis, B. R., Colwell, J. E., et al. (2011). The composition and structure of the Enceladus plume. *Geophysical Research Letters*, *38*, L11202. <https://doi.org/10.1029/2011GL047415>
- Hedman, M. M., Gosmeyer, C. M., Nicholson, P. D., Sotin, C., Brown, R. H., Clark, R. N., et al. (2013). An observed correlation between plume activity and tidal stresses on Enceladus. *Nature*, *500*(7461), 182–184. <https://doi.org/10.1038/nature12371>
- Hedman, M. M., Nicholson, P. D., Showalter, M. R., Brown, R. H., Buratti, B. J., & Clark, R. N. (2009). Spectral observations of the Enceladus plume with Cassini-VIMS. *The Astrophysical Journal*, *693*(2), 1749–1762. <https://doi.org/10.1088/0004-637X/693/2/1749>
- Hill, T. W., Thomsen, M. F., Tokar, R. L., Coates, A. J., Lewis, G. R., Young, D. T., et al. (2012). Charged nanograins in the Enceladus plume. *Journal of Geophysical Research*, *117*, A05209. <https://doi.org/10.1029/2011JA017218>
- Hurfurd, T. A., Helfenstein, P., Hoppa, G. V., Greenberg, R., & Bills, B. G. (2007). Eruptions arising from tidally controlled periodic openings of rifts on Enceladus. *Nature*, *447*(7142), 292–294. <https://doi.org/10.1038/nature05821>
- Hurfurd, T. A., Helfenstein, P., & Spitale, J. N. (2012). Tidal control of jet eruptions on Enceladus as observed by Cassini ISS between 2005 and 2007. *Icarus*, *220*(2), 896–903. <https://doi.org/10.1016/j.icarus.2012.06.022>
- Ingersoll, A. P., & Ewald, S. P. (2017). Decadal timescale variability of the Enceladus plumes inferred from Cassini images. *Icarus*, *282*, 260–275. <http://doi.org/10.1016/j.icarus.2016.09.018>
- Ingersoll, A. P., Ewald, S. P., & Trumbo, S. K. (2019). Time variability of the Enceladus plumes: Orbital periods, decadal periods, and aperiodic change. *Icarus*. <https://doi.org/10.1016/j.icarus.2019.06.006>
- Johnson, R. E., Smith, H. T., Tucker, O. J., Liu, M., Burger, M. H., Sittler, E. C., & Tokar, R. L. (2006). The Enceladus and OH tori at Saturn. *The Astrophysical Journal*, *644*(2), L137–L139. <https://doi.org/10.1086/505750>
- Kempf, S., Beckmann, U., & Schmidt, J. (2010). How the Enceladus dust plume feeds Saturn's E ring. *Icarus*, *206*(2), 446–457. <https://doi.org/10.1016/j.icarus.2009.09.016>
- Morooka, M. W., Wahlund, J.-E., Eriksson, A. I., Farrell, W. M., Gurnett, D. A., Kurth, W. S., et al. (2011). Dusty plasma in the vicinity of Enceladus. *Journal of Geophysical Research*, *116*, A12221. <https://doi.org/10.1029/2011JA017038>
- Nimmo, F., Porco, C., & Mitchell, C. (2014). Tidally modulated eruptions on Enceladus: Cassini ISS observations and models. *Astronomy Journal*, *148*(3), 46. <https://doi.org/10.1088/0004-6256/148/3/46>
- Nimmo, F., Spencer, J. R., Pappalardo, R. T., & Mullen, M. E. (2007). Shear heating as the origin of the plumes and heat flux on Enceladus. *Nature*, *447*(7142), 289–291. <https://doi.org/10.1038/nature05783>
- Omidi, N., Tokar, R. L., Averkamp, T. F., Gurnett, D. A., Kurth, W. S., & Wang, Z. (2012). Flow stagnation at Enceladus: The effects of neutral gas and charged dust. *Journal of Geophysical Research*, *117*, A06230. <https://doi.org/10.1029/2011JA017488>
- Perry, M. E., Teolis, B. D., Hurley, D. M., Magee, B. A., Waite, J. H., Brockwell, T. G., et al. (2015). Cassini INMS measurements of Enceladus plume density. *Icarus*, *257*, 139–162. <https://doi.org/10.1016/j.icarus.2015.04.037>
- Persoon, A. M., Gurnett, D. A., Kurth, W. S., Hospodarsky, G. B., Groene, J. B., Canu, P., & Dougherty, M. K. (2005). Equatorial electron density measurements in Saturn's inner magnetosphere. *Geophysical Research Letters*, *32*, L23105. <https://doi.org/10.1029/2005GL024294>
- Persoon, A. M., Gurnett, D. A., Leisner, J. S., Kurth, W. S., Groene, J. B., & Faden, J. B. (2013). The plasma density distribution in the inner region of Saturn's magnetosphere. *Journal of Geophysical Research: Space Physics*, *118*, 2970–2974. <https://doi.org/10.1002/jgra.50182>
- Persoon, A. M., Gurnett, D. A., Santolik, O., Kurth, W. S., Faden, J. B., Groene, J. B., et al. (2009). A diffusive equilibrium model for the plasma density in Saturn's magnetosphere. *Journal of Geophysical Research*, *114*, A04211. <https://doi.org/10.1029/2008JA013912>
- Porco, C., DiNino, D., & Nimmo, F. (2014). How the geysers, tidal stresses, and thermal emission across the south polar terrain of Enceladus are related. *Astronomy Journal*, *148*(3), 45. <https://doi.org/10.1088/0004-6256/148/3/45>
- Porco, C. C., Helfenstein, P., Thomas, P. C., Ingersoll, A. P., Wisdom, J., West, R., et al. (2006). Cassini observes the active south pole of Enceladus. *Science*, *311*(5766), 1393–1401. <https://doi.org/10.1126/science.1123013>
- Sakai, S., Cravens, T. E., Omid, N., Perry, M. E., & Waite, J. H. Jr. (2016). Ion energy distributions and densities in the plume of Enceladus. *Planetary and Space Science*, *130*, 60–79. <https://doi.org/10.1016/j.pss.2016.05.007>
- Saur, J., Schilling, N., Neubauer, F. M., Strobel, D. F., Simon, S., Dougherty, M. K., et al. (2008). Evidence for temporal variability of Enceladus' gas jets: Modeling of Cassini observations. *Geophysical Research Letters*, *35*, L20105. <https://doi.org/10.1029/2008GL035811>
- Shafiq, M., Wahlund, J.-E., Morooka, M. W., Kurth, W. S., & Farrell, W. M. (2011). Characteristics of the dust-plasma interaction near Enceladus' south pole. *Planetary and Space Science*, *59*(1), 17–25. <https://doi.org/10.1016/j.pss.2010.10.006>
- Smith, H. T., Johnson, R. E., Perry, M. E., Mitchell, D. G., McNutt, R. L., & Young, D. T. (2010). Enceladus plume variability and the neutral gas densities in Saturn's magnetosphere. *Journal of Geophysical Research*, *115*, A10252. <https://doi.org/10.1029/2009JA015184>
- Smith-Konter, B., & Pappalardo, R. T. (2008). Tidally driven stress accumulation and shear failure of Enceladus' tiger stripes. *Icarus*, *198*(2), 435–451. <https://doi.org/10.1016/j.icarus.2008.07.005>
- Spencer, J. (2013). Saturn's tides control Enceladus' plume. *Nature*, *500*(7461), 155–156. <https://doi.org/10.1038/nature12462>
- Teolis, B. D., Perry, M. E., Hansen, C. J., Waite, J. H., Porco, C. C., Spencer, J. R., & Howett, J. A. (2017). Enceladus plume structure and time variability: Comparison of Cassini observations. *Astrobiology*, *17*(9), 926–940. <https://doi.org/10.1089/ast.2017.1647>
- Tokar, R. L., Johnson, R. E., Thomsen, M. F., Wilson, R. J., Young, D. T., Cray, F. J., et al. (2009). Cassini detection of Enceladus' cold water-group plume ionosphere. *Geophysical Research Letters*, *36*, L13203. <https://doi.org/10.1029/2009GL038923>

- Wahlund, J.-E., Andre, M., Eriksson, A. I. E., Lundberg, M., Morooka, M. W., Shafiq, M., et al. (2009). Detection of dusty plasma near the E-ring of Saturn. *Planetary and Space Science*, *57*(14-15), 1795–1806. <https://doi.org/10.1016/j.pss.2009.03.011>
- Waite, J. H. Jr., Combi, M. R., Ip, W.-H., Cravens, T. E., McNutt, R. L. Jr., Kasprzak, W., et al. (2006). Cassini ion and neutral mass spectrometer: Enceladus plume composition and structure. *Science*, *311*(5766), 1419–1422. <https://doi.org/10.1126/science.1121290>
- Waite, J. H. Jr., Lewis, W. S., Magee, B. A., Lunine, J. I., McKinnon, W. B., Glein, C. R., et al. (2009). Liquid water on Enceladus from observations of ammonia and ⁴⁰Ar in the plume. *Nature*, *460*(7254), 487–490. <https://doi.org/10.1038/nature08153>
- Yaroshenko, V. V., Ratynskaia, S., Olson, J., Brenning, N., Wahlund, J.-E., Morooka, M., et al. (2009). Characteristics of charged dust inferred from the Cassini RPWS measurements in the vicinity of Enceladus. *Planetary and Space Science*, *57*(14-15), 1807–1812. <https://doi.org/10.1016/j.pss.2009.03.002>
- Ye, S.-Y., Gurnett, D. A., Kurth, W. S., Averkamp, T. F., Morooka, M., Sakai, S., & Wahlund, J.-E. (2014). Electron density inside Enceladus plume inferred from plasma oscillations excited by dust impacts. *Journal of Geophysical Research: Space Physics*, *119*, 3373–3380. <https://doi.org/10.1002/2014JA019861>
- Yeoh, S. K., Li, Z., Goldstein, D. B., Varghese, P. L., Levin, D. A., & Trafton, L. M. (2017). Constraining the Enceladus plume using numerical simulation and Cassini data. *Icarus*, *281*, 357–378. <https://doi.org/10.1016/j.icarus.2016.08.028>